

## ARTICLE OPEN



# Structural phase transition and superconductivity hierarchy in 1T-TaS<sub>2</sub> under pressure up to 100 GPa

Qing Dong<sup>1</sup>, Qunjun Li<sup>1</sup>, Shujia Li<sup>1</sup>, Xuhan Shi<sup>1</sup>, Shifeng Niu<sup>1</sup>, Shijie Liu<sup>1</sup>, Ran Liu<sup>1</sup>, Bo Liu<sup>1</sup>, Xuan Luo<sup>1,2</sup>, Jianguo Si<sup>2,3</sup>, Wenjian Lu<sup>1,2</sup>, Ning Hao<sup>4</sup>, Yuping Sun<sup>1,2,4,5</sup> and Bingbing Liu<sup>1</sup>

The adoption of high pressure not only reinforces the comprehension of the structure and exotic electronic states of transition metal dichalcogenides (TMDs) but also promotes the discovery of intriguing phenomena. Here, 1T-TaS<sub>2</sub> was investigated up to 100 GPa, and re-enhanced superconductivity was found with structural phase transitions. The discovered I4/mmm TaS<sub>2</sub> presents strong electron–phonon coupling, revealing a good superconductivity of the nonlayered structure. The *P*–*T* phase diagram shows a dome shape centered at ~20 GPa, which is attributed to the distortion of the 1T structure. Accompanied by the transition to nonlayered structure above 44.5 GPa, the superconducting critical temperature shows an increasing trend and reaches ~7 K at the highest studied pressure, presenting superior superconductivity compared to the original layered structure. It is unexpected that the pressure-induced re-enhanced superconductivity was observed in TMDs, and the transition from a superconductor with complicated electron-pairing mechanism to a phonon-mediated superconductor would expand the field of pressure-modified superconductivity.

*npj Quantum Materials* (2021)6:20; <https://doi.org/10.1038/s41535-021-00320-x>

## INTRODUCTION

As a major branch of two-dimensional materials, transition metal dichalcogenides (TMDs) have been a research hotspot due to their exotic electronic properties<sup>1–3</sup>. Layered TMDs share a common X–M–X sandwich structure (*M* = Mo, W, Nb, Ti, Ta, etc.; *X* = S, Se, Te); the X–M–X trilayers stack together via weak van der Waals (vdW) interactions, resulting in a wide variety of polymorphs, such as 1T, 1T', *T*<sub>d</sub>, 2H, and 3R. 1T-TaS<sub>2</sub>, as a rare TMD that has both the Mott state and multiple charge-density-wave (CDW) phases<sup>4–6</sup>, has attracted much attention. The peculiar properties of the Mott state and CDW phases have been thoroughly studied by introducing external parameters, such as disorder<sup>7</sup>, doping<sup>8,9</sup>, thickness variation<sup>10,11</sup>, and photoelectric fields<sup>12–14</sup>. The electron–phonon and electron–electron interactions are considered to play an equal role in the extraordinary features of 1T-TaS<sub>2</sub>.

Pressure, as a powerful tool for continuously tuning crystal and electronic structures away from pristine states, has been widely utilized in TMDs. As the interlayer spacing decreases during compression, the bandgap of semiconducting TMDs will decrease until total closure<sup>15–17</sup>. Pressure also provides a clean way to discern the interaction between CDWs and superconductivity in TMDs. The dome-shaped *P*–*T* phase diagrams, which are sensitive to the collapse of CDWs, indicate that superconductivity competes with CDWs<sup>18,19</sup>. In other cases, the superconducting critical temperature (*T*<sub>c</sub>) under pressure either remains constant or increases regardless of the change in the CDWs, indicating that CDWs are weakly connected to superconductivity<sup>20,21</sup>. In terms of the recently concerned Weyl semimetal TMDs, enhanced superconductivity was observed in MoTe<sub>2</sub> when external pressure was applied<sup>22,23</sup>; for WTe<sub>2</sub>, the extremely large magnetoresistance at ambient conditions drastically decreased under compression, and pressure-driven superconductivity was sharply achieved<sup>24,25</sup>.

In the above studies, the changes in the electronic states were usually accompanied by an isostructural phase transition or structural lattice distortion. Obviously, pressure broadens our views of the structures and electronic properties of 2D materials.

Plentiful electronic state changes occur in 1T-TaS<sub>2</sub> under high pressure. Superconductivity was found in compressed 1T-TaS<sub>2</sub><sup>20</sup>; the interplay of CDWs and superconductivity was analyzed using different methods. Superconductivity in 1T-TaS<sub>2</sub> was attributed to the separated metallic interdomain in real space<sup>20</sup>. Density functional calculations confirmed that pressure suppresses the CDW instability and stabilizes the interdomain phase<sup>26</sup>. X-ray diffraction (XRD) studies proved that the increasing pressure would gradually result in a transformation to a normally unmodulated structure in 1T-TaS<sub>2</sub>, but the authors also proposed that the superconducting and the CDW gap exist in separate regions of reciprocal space<sup>27,28</sup>. Recently, superconductivity was found in the semiconducting 2H-MoS<sub>2</sub> at ~90 GPa, and *T*<sub>c</sub> rapidly increases to above 10 K and stabilizes at ~12 K over a wide pressure range up to 220 GPa<sup>29</sup>. Theoretical calculations of ReS<sub>2</sub> predicted a tetragonal superconducting I4<sub>1</sub>/amd structure at approximately 90 GPa, and the superconductivity was confirmed by electrical resistance measurements<sup>30</sup>. The above studies reveal that abundant crystal and electronic structure changes occur in TMDs under high pressure. However, the previous studies on 1T-TaS<sub>2</sub> are limited to the low-pressure region, and the impact of structural changes on the electronic states has not been considered, which precludes our understanding of the extraordinary properties of TMDs. In this study, we extended the high-pressure research on 1T-TaS<sub>2</sub> up to ~100 GPa. Details of the high-pressure experiments and the theoretical calculations were summarized in the Supplementary Information. Three structural phase transitions and *P*–*T* phase diagram of TaS<sub>2</sub> are proposed.

<sup>1</sup>State Key Laboratory of Superhard Materials, Jilin University, Changchun, China. <sup>2</sup>Key Laboratory of Materials Physics, Institute of Solid State Physics, Chinese Academy of Sciences, Hefei, China. <sup>3</sup>University of Science and Technology of China, Hefei, China. <sup>4</sup>Anhui Province Key Laboratory of Condensed Matter Physics at Extreme Conditions, High Magnetic Field Laboratory, Chinese Academy of Sciences, Hefei, China. <sup>5</sup>Collaborative Innovation Center of Advanced Microstructures, Nanjing University, Nanjing, China. ✉email: liquanjun@jlu.edu.cn; ypsun@issp.ac.cn; liubb@jlu.edu.cn

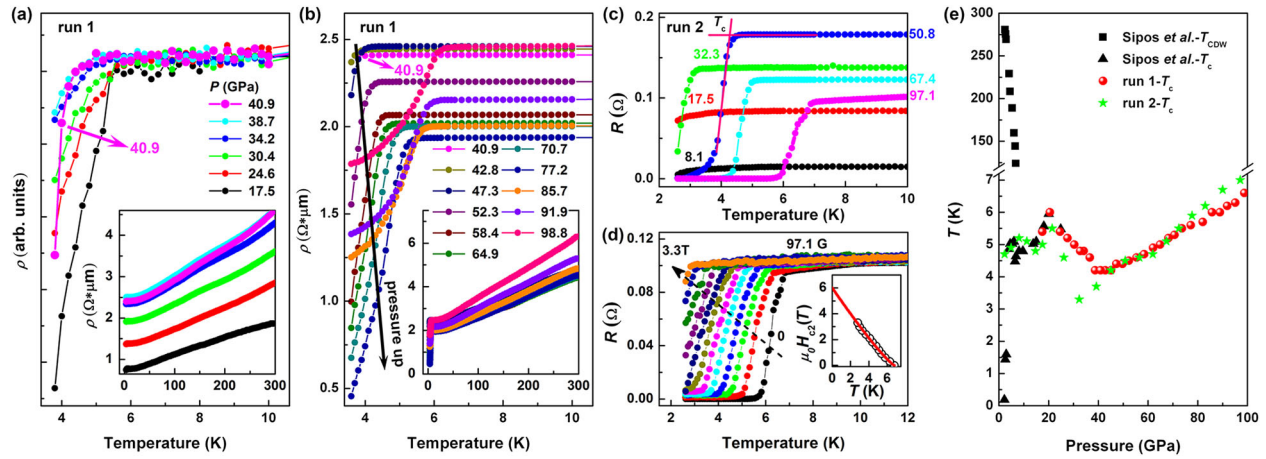


**Fig. 1 Pressure-induced superconductivity in 1T-TaS<sub>2</sub>.** Temperature-dependent resistivity under pressures ranging from **a** 17.5 to 40.9 GPa (normalized to the same magnitude at elevated pressures) and **b** 40.9 to 98.8 GPa in run 1. **c** Temperature-dependent resistance curves under high pressure in run 2. Zero resistance has been measured since 50.8 GPa. **d** shows the  $R$ - $T$  curve under increasing magnetic field at 97.1 GPa. The criterion for determining  $T_c$  in two runs is shown in **c**. Inset of **d** plots the best fit of  $T_c$  vs  $H$  using the empirical formula  $H_{c2}(T) = H_{c2}^*(1 - T/T_c)^{1 + \alpha}$ . **e** Temperature–pressure phase diagram of TaS<sub>2</sub>; the black solid squares and triangles represent the  $T_{CDW}$  and  $T_c$  from previous electrical resistivity measurements<sup>20</sup>. The red solid circles and green stars represent the  $T_c$  measured in this study.

Enhanced superconductivity with a layered-to-nonlayered structural transition, and the transformation from a superconductor with complicated electron-pairing mechanism to a phonon-mediated superconductor, were found. The relationship between the structures and superconductivity of TaS<sub>2</sub> is discussed.

## RESULTS

### Superconductivity under high pressure

The electronic transport measurements on 1T-TaS<sub>2</sub> were carried out twice. Figure 1a, b show the temperature-dependent resistivity of TaS<sub>2</sub> under pressures ranging from 17.5 to 98.8 GPa in run 1. Superconductivity is found over the whole pressure range; the system is fully metallic above the critical temperature  $T_c$ . As shown in Fig. 1a, when the pressure increases from 17.5 to 38.7 GPa, the superconducting trend becomes flatter, indicating a reduction of the superconductivity. However, as the pressure increases to 40.9 GPa, the superconducting trend suddenly becomes steeper (magenta line, Fig. 1a). Upon further compression, a remarkable superconductivity can be identified (Fig. 1b). To further verify the superconductivity of TaS<sub>2</sub>, the low-temperature electrical resistance measurements in a pressure range of 2.3–97.1 GPa in run 2 were conducted (The whole pressure-dependent  $R$ - $T$  curves are shown in Supplementary Fig. 3). At the low-pressure range, the strong upturn in resistance that signals the CDW transition, as shown in Supplementary Fig. 3a, becomes less pronounced as pressure increases. Upon the compression to 8.1 GPa, it can be seen that the system is fully metallic and the CDW finally collapses, which is consistent with previous study<sup>20</sup>. Zero resistance has been measured since 50.8 GPa as illustrated in Fig. 1c. Upon further compression, the zero resistance transition temperature ( $T_{zero}$ ) increases and the superconductivity of the entire system enhances. The absence of zero resistance at low-temperature range could be attributed to that a pressure gradient throughout the sample due to the nonhydrostatic pressure condition broadens the superconducting transition. The criterion for determining  $T_c$  in two runs is shown in Fig. 1c. Supplementary Fig. 4 displays the pressure dependence of the superconducting transition width  $\Delta T$  (defined as  $T_c - T_{zero}$ ) in run 2. As the pressure increases,  $\Delta T$  is almost independent of pressure and fluctuates around 1.5–1.9 K.

Measurements of resistance around  $T_c$  for various external magnetic fields were also carried out in run 2. The zero-resistance state at 97.1 GPa gradually lifted with increasing field, resulting in a decrease in  $T_c$  (Fig. 1d). This gave complimentary evidence of the superconducting state. As shown in the inset of Fig. 1d, the upper critical field ( $H_{c2}(T)$ ) has a positive curvature close to  $T_c$  ( $H = 0$ ), which is deviated from the Werthamer–Helfand–Hohenberg theory based on the single-band mode. The experimental data  $H_{c2}(T)$  were appropriately fitted using the empirical formula  $H_{c2}(T) = H_{c2}^*(1 - T/T_c)^{1 + \alpha}$ . The estimated value of  $H_{c2}(0)$  at various pressures are summarized in Supplementary Fig. 5c, presenting an increasing tendency with increasing pressure, which is similar to the  $T_c$  trend. The irreversibility line of TaS<sub>2</sub> was obtained by using a resistance criterion of 5% $R_n$  ( $R_n$  is the resistance of normal state above  $T_c$ ), as established in the high  $T_c$  superconductors. The variations of irreversibility field  $H_{irr}$  as a function of temperature at elevated pressures are displayed in Supplementary Fig. 6. As the pressure increases, the irreversibility line shifts to a higher temperature and higher magnetic field, revealing the robust superconductivity of TaS<sub>2</sub> with increasing pressure.

### $T_c$ evolution under pressure

Figure 1e summarizes our findings in a pressure–temperature phase diagram together with previous electrical resistivity measurements. The  $T_c$  trends in two runs show the similarity. The  $T_c$  variations with pressure below 25 GPa are in line with previous research<sup>20</sup>. A superconductivity dome appears in the range of 2.5–40 GPa around the critical pressure of ~20 GPa, where  $T_c$  reaches a peak value of 6 K. This superconductivity dome was not observed in previous research due to the limited pressure range. The  $T_c$  in run 1 decreases to 4.2 K at 38.7 GPa, while in run 2,  $T_c$  reaches 3.3 K at 32.3 GPa. Above ~45 GPa, both  $T_c$  presents a slowly but firmly upward trend. The highest  $T_c$  in our experiments is ~7 K in the limited pressure range. As illustrated in the trend of the  $P$ - $T$  diagram,  $T_c$  will increase further if higher pressure is applied. Pressure-induced superconductivity has been found in several TMDs<sup>18–22,25</sup>. Among all these studies,  $T_c$  usually attains the maximum at an optimal pressure rapidly and then either remains constant or drops. The re-enhancement of  $T_c$  under high pressure has not been found in TMDs.

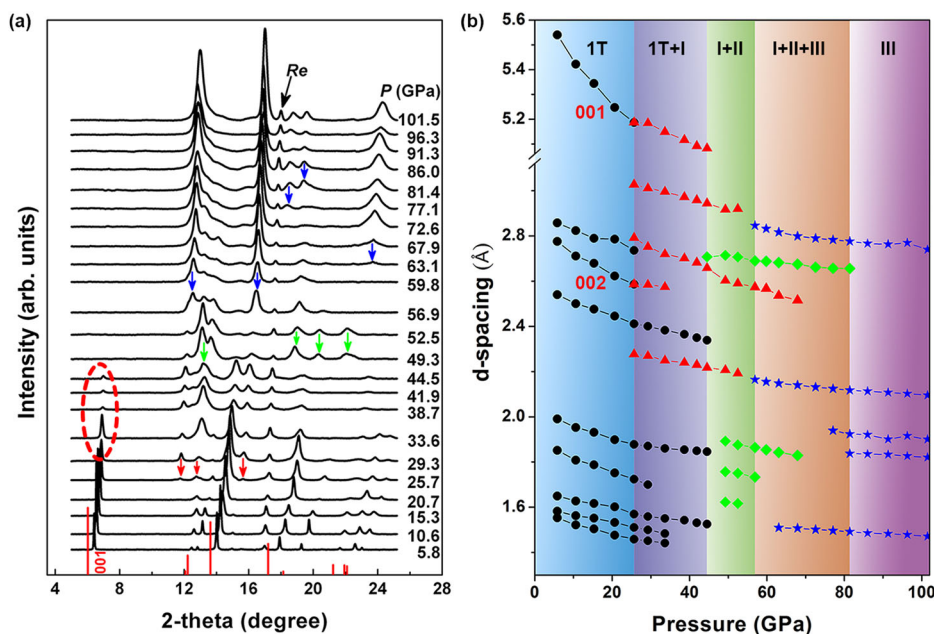


**Fig. 2** Structure evolution under pressure. **a** Synchrotron Angle Dispersive X-ray Diffraction (ADXRD) patterns for 1T-TaS<sub>2</sub> up to 101.5 GPa. The red sticks represent the peaks of the original 1T structure. The red/green/blue arrows mark the appearance of new Bragg peaks. The black arrow marks the (101) peak of Reused as a gasket. **b** Evolution of d-spacing with increasing pressure.

### Fitting of $R$ - $T$ and $\rho$ - $T$ curves

The normal states above  $T_c$  in two runs were fitted by the empirical formula of  $\rho(T) \approx \rho_0 + AT^n$  and  $R(T) \approx R_0 + AT^n$ , where  $\rho_0$  and  $R_0$  are the residual resistivity and residual resistance, the prefactor  $A$  and the exponent  $n$  are related to the inelastic electron scattering. The pressure dependences of  $\rho_0$ ,  $R_0$ ,  $A$ , and  $n$  are displayed in Supplementary Fig. 7. The fitted value of  $R_0$  in run 2 decreases rapidly in the pressure range of 2.3–8.1 GPa, which can be attributed to the collapse of CDW. In the high-pressure range, the residual resistivity in run 1 and the residual resistance in run 2 both show an increasing trend at first and then turn into a downward trend under high pressure. The pressure dependences of  $\rho_0$  and  $R_0$  are opposite to that of  $T_c$  at the pressure interval of 20–82.1 GPa. The difference is that, above 82.1 GPa, the decreasing  $\rho_0$  trend in run 1 reverse but the decreasing  $R_0$  trend in run 2 does not. The different behavior of  $\rho_0$  and  $R_0$  above 82.1 GPa may come from the diverse nonhydrostatic pressure condition when the applied pressure is very high. The exponent  $n$  in both two runs was estimated by fitting the temperature range from  $T_c$  up to 35 K. In run 2, the fitted value of  $n$  below 8.1 GPa is less than 2, showing a non-Fermi liquid behavior. In much higher pressure range,  $n$  in both two runs fluctuates between 2.5 to 3.5, different from the value of  $n = 2$  for electron–electron or  $n = 5$  for electron–phonon scattering. This rather unusual temperature exponent is commonly attributed to a phonon-assisted  $s$ - $d$  interband scattering.

### Structure evolution under high pressure

The Angle Dispersive X-ray Diffraction (ADXRD) patterns shown in Fig. 2a were collected up to 101.5 GPa, and the evolution of the d-spacing is presented in Fig. 2b. Three structural transitions are confirmed at 25.7, 44.5, and 56.9 GPa, which we name phase I, phase II, and phase III temporarily. The first pattern is taken at 5.8 GPa, and all peaks can be attributed to the 1T structure. The original 1T phase is retained up to 20.7 GPa. The (001) and (002) peaks show faster compressive behaviors than the other peaks. The value of the (001) peak represents the distance between adjacent layers. Apparently, the 1T structure is more compressible along the  $c$ -axis due to the weak vdW interactions between the

sulfur–sulfur layers along this direction. Upon compression to 25.7 GPa, three new peaks marked by the red arrows suddenly appear, indicating the onset of a structural transition. The original (001) and (002) peaks show discontinuous compression ratio above 25.7 GPa, indicating that the 1T structure partially transforms into phase I. With continuous compression to 41.9 GPa, the intensity of the new peaks strengthens, while the intensity of the original 1T structure peaks weakens, and some peaks even disappear. As the pressure increases up to 44.5 GPa, a new peak (marked by the green arrow) splits from a phase I peak, and the transition to phase II occurs. Meanwhile, all diffraction peaks that belong to the original 1T structure vanish. Three more new peaks appear at 49.3 GPa (marked by the green arrows), and they are classified as phase II peaks. With a continuous increase in the pressure to 56.9 GPa, phase III suddenly arises, with two peaks appearing at 2.85 Å and 2.16 Å. In the pressure range from 56.9 GPa to 81.4 GPa, three more new phase III peaks appear (marked by the blue arrows); the intensity of these peaks is rapidly enhanced with increasing pressure, while the diffraction peaks of phases I and II gradually weaken and disappear. Above 81.4 GPa, the phase III peaks dominate the ADXRD spectra.

### DISCUSSION

In the pressure range from 25.7 to 56.9 GPa, the system is always in a mixed-phase state among 1T, phase I and phase II. Although confirming the precise structures of phases I and II are difficult, some features can still be speculated based on the XRD patterns. As illustrated in Fig. 2b, two phase I peaks derive from the original 1T structure. The (001) peak in the 1T structure represents the distance between adjacent layers. The inheritance of the (001) peak suggests that phase I is also a layered structure. The structural transition to phase I should result from the pressure-induced distortion of the 1T structure. In layered TMDs, the cell parameter  $c$  is more compressible than  $a$  or  $b$ . Previous studies consider that 2D to 3D structural transformation occurs when  $c$  decreases to a limitation<sup>16,17</sup>. While in our measurements, the change of (001) peak is obviously more representative to expose the 3D structure transition. Above 38.7 GPa, a clear reduction in

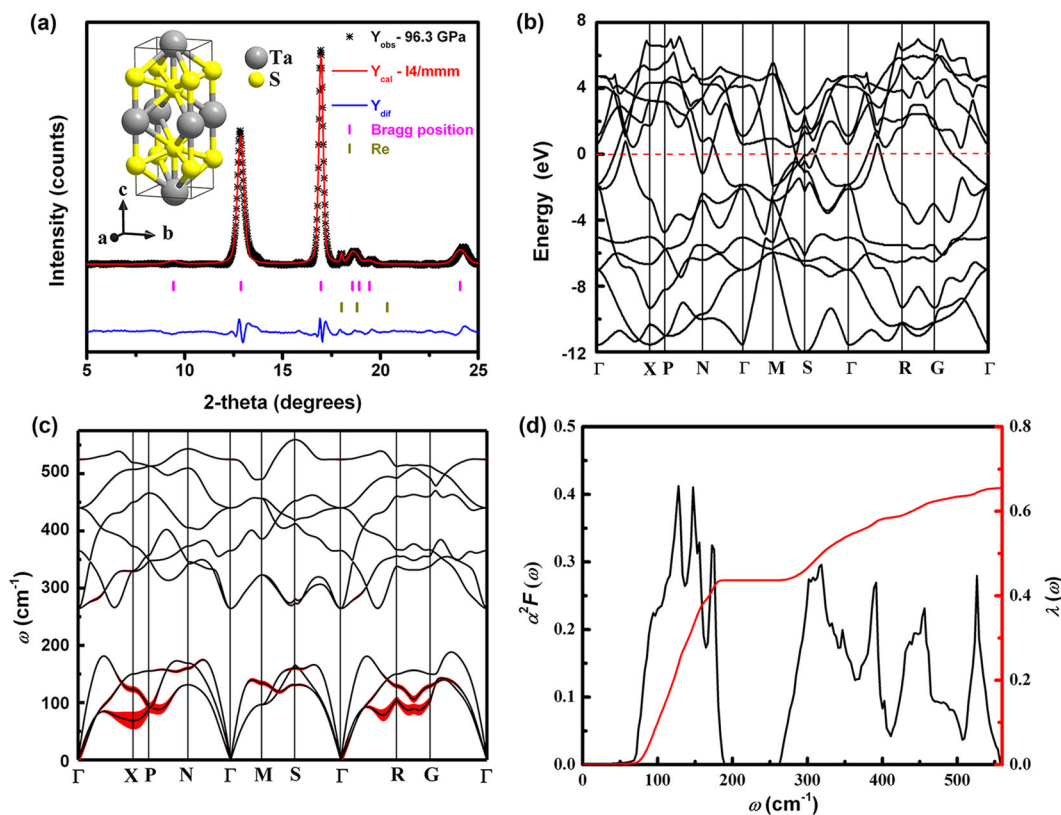


**Fig. 3** Crystal structure and electronic states of  $I4/mmm$  phase. **a** Rietveld refinement of XRD data taken at 96.3 GPa using the  $I4/mmm$  structure. The inset of **a** shows the structure of  $I4/mmm$   $TaS_2$ . **b** Calculated band structure and **c** calculated phonon dispersion of the  $I4/mmm$  phase at 90 GPa. The red dashed line shows the Fermi level ( $E_F$ ). The red areas show the electron–phonon coupling (EPC), with the width proportional to the respective strength. **d** Eliashberg spectral function,  $\alpha^2F(\omega)$  (left vertical axis), and electron–phonon integral,  $\lambda(\omega)$  (right vertical axis).

the original (001) peak is observed (emphasized by the red dotted oval in Fig. 2a). Accompanied by the distorted (001) peak totally disappearing, phase II occurs at 44.5 GPa. Any peak with large  $d$ -spacing that can represent the layer spacing never appears again. We conjecture that the weak interlayer vdW force gradually changes into strong sulfur–sulfur covalent bonding with continuous compression, and the layered structure eventually transforms into a nonlayered structure at 44.5 GPa. Phase II should be the first nonlayered structure.

As for phase III, it is the only  $TaS_2$  structure surviving above 81.4 GPa. An  $I4/mmm$  structure was proposed based on a global minimization of the free-energy surfaces combined with the particle swarm optimization methodology as implemented in the CALYPSO (crystal structure AnaLYsis by Particle Swarm Optimization) code<sup>31,32</sup>. Rietveld refinement of the XRD data taken at 96.3 GPa using the  $I4/mmm$  structure is illustrated in Fig. 3a. The perfect match of the theoretical pattern with the experimental data indicates that phase III belongs to the  $I4/mmm$  structure. The detailed structural parameters of the  $I4/mmm$  structure are summarized in Supplementary Table 1. As presented in the inset of Fig. 3a, the  $I4/mmm$  phase is a nonlayered structure. Returning to the discussion on phase II, we find that phase II can be sustained only over a short pressure interval and soon transforms into the nonlayered  $I4/mmm$  phase. This finding further proves that phase II is a nonlayered mesophase between the layered structure and the ultimately stable nonlayered  $I4/mmm$  phase. The XRD patterns in the decompression process are shown in Supplementary Fig. 8. Upon the decompression to 36.8 GPa, the peak which represents the distance between adjacent layers in layered TMDs reappears, indicating that  $TaS_2$  transforms back into

the layered structure in the decompression process. As the pressure decreases to atmospheric conditions, the nonlayered  $I4/mmm$  phase totally collapsed. Although the XRD pattern decompressed to 0 GPa cannot show the characteristic of original layered 1T structure due to the few and weak peaks, we can still speculate that the pressure-induced layered to nonlayered structural transition in  $TaS_2$  is reversible.

We further calculated the band structure, electron–phonon coupling (EPC), phonon dispersion, Eliashberg spectral function  $\alpha^2F(\omega)$ , and electron–phonon integral  $\lambda(\omega)$  of  $I4/mmm$   $TaS_2$  at 90 GPa with density functional perturbation theory<sup>33</sup>, as shown in Fig. 3b–d. The calculation details can be found in Supplementary Information. The red areas in the phonon dispersion illustrate the strong EPC in the  $I4/mmm$  structure. The EPC constant  $\lambda$ <sup>34</sup> reaches 0.65 at 90 GPa, and the  $T_c$  estimated using the Allen–Dynes-modified McMillan formula is  $\sim 7.6$  K. As illustrated in Fig. 1e, our calculated  $T_c$  agrees reasonably well with the experimental results.

Overall, a series of transitions, from the 1T structure to “distorted 1T”, then a metastable “nonlayered” structure, and finally the nonlayered tetragonal  $I4/mmm$  structure, were found in the compressed  $TaS_2$ . A layered-to-nonlayered tetragonal structure transition has been consistently predicted in layered TMDs<sup>35–39</sup>, regardless of 2H, 1T, 1T’, etc. Some calculations even suggested potential superconductivity for the nonlayered tetragonal structure. Recently, Chi et al. found that  $MoS_2$  retains the  $2H_a$  structure up to  $\sim 155$  GPa with remarkable superconductivity<sup>29</sup>, which was attributed to the emergence of a new flat Fermi pocket in the electronic structure. This result is very different from the theoretical calculation<sup>40</sup>; nonlayered tetragonal structure predictions seem inapplicable to 2H structure TMDs. Zhou et al. predicted a

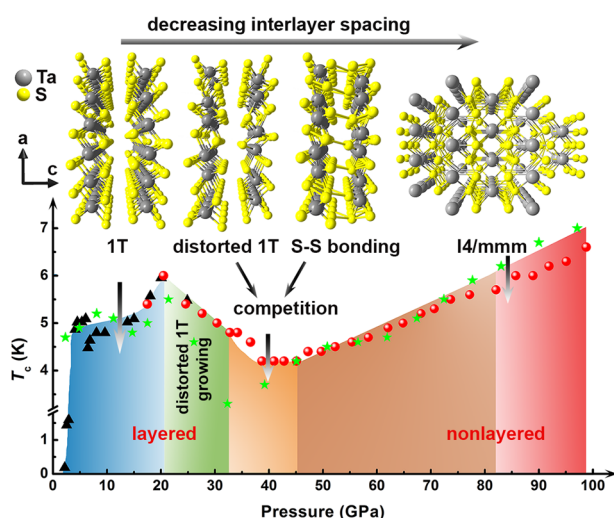


**Fig. 4 Schematic diagram of the structural changes in TaS<sub>2</sub> under compression and the  $T_c$  variation with pressure.** The  $P$ - $T_c$  diagram is divided into different regions based on the structural transitions under high pressure. The black solid triangles represent  $T_c$  from previous electrical resistivity measurements<sup>20</sup>. The red solid circles and green stars represent the  $T_c$  measured in run 1 and run 2, respectively.

superconducting tetragonal I4<sub>1</sub>/amd structure for 1T'-ReS<sub>2</sub>, and the superconducting phase transition was confirmed by high-pressure electrical resistance measurements<sup>30</sup>. Regrettably, no substantial evidence, such as XRD patterns, currently verifies the I4<sub>1</sub>/amd structure. In our measurements, the perfect match of the theoretical pattern with experimental data demonstrates that the original layered 1T structure of TaS<sub>2</sub> transforms into the nonlayered I4/mmm structure. Our findings verify the nonlayered tetragonal structure transition for 1T structure TMDs; the transition sequence of TaS<sub>2</sub> also suggests a way to investigate the structural change for 1T structure TMDs. As illustrated in Fig. 1, the nonlayered structure presents more prominent superconductivity and relatively higher  $T_c$  than the layered structure, which would inspire more experiments and theoretical calculations on other TMDs.

A comparison between the pressure dependences of the  $d$ -spacing and  $T_c$  is shown in Supplementary Fig. 9. Figure 4 summarizes the structural phase transitions and the  $T_c$  variation of TaS<sub>2</sub> under high pressure. In the low-pressure region,  $T_c$  reaches a peak of 6 K at ~20 GPa and then drops. The dome-shaped  $P$ - $T$  diagram shows similarity to other CDW TMDs, whose domes were attributed to the competition between CDWs and superconductivity<sup>18,19</sup>. For 1T-TaS<sub>2</sub>, although no consensus on when CDWs disappear has been reached among numerous high-pressure studies, the generally accepted opinion is that pressure suppresses CDWs<sup>20,27,28</sup>. Our electrical resistance measurements at the low-pressure range in run 2 clearly show that the CDW in 1T-TaS<sub>2</sub> finally collapses around 8.1 GPa (Supplementary Fig. 3a). So, the influence of CDW on the  $T_c$  variation above 8.1 GPa can be excluded. The XRD patterns show that 20.7 GPa is the last pressure point at which the pure 1T structure occurs. As the pressure increases, the original 1T structure disappears, the "distorted 1T" structure grows, and the  $T_c$  of the entire system gradually decreases. Based on this, we attribute the  $T_c$  variation at ~20 GPa to the distortion of the 1T structure. The "distorted 1T" structure presents weaker superconductivity.

The downtrend of  $T_c$  ceases at 38.7 GPa in run 1, which stops at 32.3 GPa in run 2. After the  $T_c$  reaches a minimum at the certain pressures, the  $T_c$  trends in two runs both show an increasing tendency. The difference of the  $T_c$  upturn pressures in two runs can be contributed to the pressure error caused by the

nonhydrostatic condition in electronic transport measurements (Details of the high-pressure measurements are summarized in the Supplementary Information). It is worthy to note that the original (001) peak, which represents the interlayer spacing of TaS<sub>2</sub>, weakens significantly above 33.6 GPa (shown in Fig. 2a). A reasonable conjecture is that accompanied by the phase transitions, the weak interlayer vdW force is partly replaced by interlayer sulfur-sulfur covalent bonding above ~33.6 GPa, and the replacement is finally completed at ~44.5 GPa. Therefore, we suggest that the  $T_c$  variation in the pressure range of 32.3/38.7–44.5 GPa can be related to the layered-to-nonlayered phase transition.

Above ~45 GPa,  $T_c$  in both runs presents a slowly but firmly upward trend and reaches ~7 K in our limited pressure range. The continuous rising tendency does not stop or jump, despite the phase transition to the I4/mmm structure, at 56.6 GPa. The increasing trend also does not change even when the I4/mmm structure dominates the XRD patterns above 81.4 GPa. In other pressure-induced superconducting TMDs,  $T_c$  usually rises over a narrow pressure range and then either remains constant or drops<sup>18,19,21,22,25,41</sup>. In our case, the  $T_c$  maintains the rising tendency over a wide pressure range, presenting a more prominent capability for controlling the superconductivity. Inspecting the phase diagram in Fig. 4, we find that the  $T_c$  enhancement is initiated with the system transforming from a 2D layered structure into a 3D nonlayered structure, indicating a close relationship to the pressure-induced structural phase transition. As an only known high-pressure phase, investigation of the electronic state on I4/mmm structure is of great importance in revealing the  $T_c$  enhancement. The density of states of nonlayered I4/mmm structure was calculated and compared with that of layered 1T structure (shown in Supplementary Fig. 10). As can be seen, the Fermi surface of 1T structure is mainly composed of the  $d$  orbital of Ta atoms, while for I4/mmm phase, the  $d$  orbital of Ta atoms and the  $p$  orbital of S atoms contribute equally. The DFT calculations indicate the multi-band superconductivity (MBCS) for the I4/mmm phase. A similar MBCS was also found in the layered s-wave superconductor NbSe<sub>2</sub><sup>42,43</sup>.

We further calculated the  $T_c$  of I4/mmm structure at different pressures based on BCS theory, finding that the  $T_c$  variation presents a decreasing tendency, which is different from the experimental results (Supplementary Figs. 11 and 12). Obviously, the pressure-dependent superconductivity of I4/mmm phase cannot be simply explained within the framework of the electron-phonon coupling mechanism, some other factors also work on it. XRD measurement shows that TaS<sub>2</sub> undergoes a series of structural transitions under high pressure, and the nonlayered I4/mmm structure becomes the dominant phase above 81.4 GPa. Thus,  $T_c$  of the entire system above 81.4 GPa is approximately equal to the superconducting transition temperature of the I4/mmm phase. Below 81.4 GPa, the system is in a mix-phase state of I4/mmm structure and other phases. As the mix-phase increases, disorder of the whole system increases too and the interband scattering between the  $d$  orbital of Ta atoms and the  $p$  orbital of S atoms enhances, which will suppress  $T_c$ . With increasing pressure in our measurement, the disorder drops as the mix-phase transforms into the pure I4/mmm structure, which contributes to the  $T_c$  enhancement above ~45 GPa. Returning to the discussion on pressure-dependent residual resistivity in Supplementary Fig. 7a,  $\rho_0$  remains almost constant at the pressure interval of 34.2–45.1 GPa can also be well explained by the competition between multiple phases. Above 82.1 GPa,  $\rho_0$  turns into an increasing trend and simultaneously I4/mmm phase becomes the dominant structure. Thus, the influence of mix phase can be excluded. The increase of  $\rho_0$  above 82.1 GPa results from the intrinsic property of I4/mmm structure.

As is well known, 1T-TaS<sub>2</sub> attracted numerous researches due to its numbers of peculiar CDW phases. Pressure-induced superconductivity in the original 1T structure was always entangled

with the CDW phases<sup>28</sup>, and the conventional electron–phonon interaction cannot explain the superconductivity<sup>26</sup>, which indicates that the other complicated superconducting pairing mechanisms may be included, except the traditional EPC, in the 1T structure. The emerged superconductivity in compressed or copper doped 1T-TaS<sub>2</sub> around a new type of quantum critical point (QCP) is another example of unconventional superconductivity in CDW-related TMDs<sup>19,44</sup>. Astonishingly, when the external pressure was applied, TaS<sub>2</sub> transforms from a 1T structure to an I4/mmm phase finally, whose superconductivity can be properly illustrated by strong EPC. This indicates that the other superconducting pairing mechanisms are precluded and the EPC becomes the dominant driving force for the Cooper pairing in TaS<sub>2</sub> under ultra-high pressure. As far as we know, this type of transition has not been observed. Although the superconducting mechanism in TaS<sub>2</sub> still needs to be explored further both theoretically and experimentally, our results bring up an unnoticed research field on the transition from unconventional to conventional superconducting state stimulated by external pressure, electronic field, etc.

In summary, structural phase transitions and the abundant  $T_c$  variation of TaS<sub>2</sub> under high pressure are reported. A series of transitions, from the 1T structure to “distorted 1T”, then a metastable “nonlayered” structure, and finally the nonlayered tetragonal I4/mmm structure, were found. The I4/mmm structure presents superior superconductivity compared to the original layered structure, and the strong EPC reveals the prominent superconductivity of the nonlayered structure.  $T_c$  reaches a peak value of 6.0 K at ~20 GPa and then drops, which can be attributed to the distortion of the 1T structure. After the superconductivity recession, a re-enhanced superconductivity emerges over a large pressure range; above ~45 GPa,  $T_c$  presents an increasing trend and reaches ~7 K at the highest studied pressure of about 100 GPa. It is unexpected that the pressure-induced re-enhanced superconductivity was observed in the TMDs. Our findings deeply enrich the view on the structural changes and electronic states of TMDs, which will motivate further experimental and theoretical studies on TMDs to explore the enhanced superconducting phases. The transition from a superconductor with complicated electron-pairing mechanism to a phonon-mediated superconductor in compressed 1T-TaS<sub>2</sub> would expand the field of pressure-modified superconductivity.

## METHODS

### Single crystal growth

High-quality single crystals of 1T-TaS<sub>2</sub> were grown by the chemical vapor transport (CVT) method with iodine as a transport agent. The high-purity Ta (3.5 N) and S (3.5 N) were mixed in chemical stoichiometry and heated at 850 °C for 4 days in an evacuated quartz tube. The harvested TaS<sub>2</sub> powders and iodine were then sealed in another quartz tube and heated for 2 weeks in a two-zone furnace, in which the source zone and growth zone were fixed at 900 °C and 800 °C, respectively. The tubes were rapidly quenched in cold water to ensure retaining of the 1T phase.

### Details of high pressure measurements

The high pressure electronic transport measurements were conducted on a nonmagnetic diamond anvil cell (DAC) made of BeCu alloy, using the standard four-point probe method in a homemade multifunctional measurement system (2–300 K, JANIS Research Company Inc.; 0–9 T, Cryomagnetics Inc.). In situ high-pressure XRD experiments were performed at the BL15U beamline of the Shanghai Synchrotron Radiation Facility (SSRF) ( $\lambda = 0.6199 \text{ \AA}$ ). Rhenium was used as the gasket material in all high-pressure measurements. A 4:1 methanol–ethanol mixture was adopted as the pressure transmitting medium in XRD measurements, and no pressure transmitting medium was used in electrical transport measurements. The  $R_1$  fluorescence line of ruby was used to calibrate

pressures in the lower range; the Raman spectrum of diamond was employed as a pressure calibrant in the higher region. Raman spectra were collected on a micro-Raman spectrometer (HR Evolution) using a 473 nm Ar<sup>+</sup> laser as the excitation source.

## Theoretical calculations

The first-principles calculations were performed with QUANTUM ESPRESSO (QE) package based on the density functional theory (DFT) and the density functional perturbation theory (DFPT)<sup>33</sup>. The ultrasoft pseudopotentials were used for the calculations of electronic structure and lattice dynamics including the phonon spectrum and electron–phonon coupling<sup>45</sup>. The exchange–correlation functionals were treated by the Perdew–Burke–Ernzerhof functional<sup>46</sup>. The cutoff energy of 50 Ry and 400 Ry were set for the wave functions and the charge density, respectively. The Fermi–Dirac–smearing method with a smearing parameter of  $\sigma = 0.005$  Ry was used. The initial structures were obtained by CALYPSO (crystal structure AnaLYsis by Particle Swarm Optimization) software<sup>31,32</sup> and then relaxed them until the Hellmann–Feynman force acting on each atom was less than  $10^{-4}$  Ry/Å. The convergence criterion for self-consistent calculations was set to be  $10^{-8}$  Ry. The Brillouin zone (BZ) was sampled with a  $10 \times 10 \times 10$  mesh of  $k$  points. The phonon dispersion and electron–phonon coupling was calculated with a  $5 \times 5 \times 5$  mesh of  $q$  points. The electron–phonon matrix elements were calculated with a  $20 \times 20 \times 20$  mesh of  $k$  points. The superconducting transition temperature  $T_c$  is calculated with the Allen–Dynes-modified McMillan equation<sup>34,47</sup>.

## DATA AVAILABILITY

The authors declare that all relevant data supporting the findings of this study are available within the paper and its supplementary information files.

Received: 24 September 2020; Accepted: 28 January 2021;

Published online: 02 March 2021

## REFERENCES

1. Yokoya, T. et al. Fermi surface sheet-dependent superconductivity in 2H-NbSe<sub>2</sub>. *Science* **294**, 2518–2520 (2001).
2. Xiao, D., Liu, G. B., Feng, W. X., Xu, X. D. & Yao, W. Coupled spin and valley physics in monolayers of MoS<sub>2</sub> and other group-VI dichalcogenides. *Phys. Rev. Lett.* **108**, 196802 (2012).
3. Kang, K. et al. High-mobility three-atom-thick semiconducting films with wafer-scale homogeneity. *Nature* **520**, 656–660 (2015).
4. Scruby, C. B., Williams, P. M. & Parry, G. S. The role of charge density waves in structural transformations of 1T-TaS<sub>2</sub>. *Philos. Mag.* **31**, 255–274 (1975).
5. Wu, X. L. & Lieber, C. M. Hexagonal domain-like charge density wave phase of TaS<sub>2</sub> determined by scanning tunneling microscopy. *Science* **243**, 1703–1705 (1989).
6. Wu, X. L. & Lieber, C. M. Direct observation of growth and melting of the hexagonal-domain charge-density-wave phase in 1T-TaS<sub>2</sub> by scanning tunneling microscopy. *Phys. Rev. Lett.* **64**, 1150–1153 (1990).
7. Lahoud, E., Meetei, O. N., Chaska, K. B., Kanigel, A. & Trivedi, N. Emergence of a novel pseudogap metallic state in a disordered 2D Mott insulator. *Phys. Rev. Lett.* **112**, 206402 (2014).
8. Rossnagel, K., Rotenberg, E., Koh, H., Smith, N. V. & Kipp, L. Continuous tuning of electronic correlations by alkali adsorption on layered 1T-TaS<sub>2</sub>. *Phys. Rev. Lett.* **95**, 126403 (2005).
9. Ang, R. et al. Real-space coexistence of the melted Mott state and superconductivity in Fe-substituted 1T-TaS<sub>2</sub>. *Phys. Rev. Lett.* **109**, 176403 (2012).
10. Hovden, R. et al. Atomic lattice disorder in charge-density-wave phases of exfoliated dichalcogenides (1T-TaS<sub>2</sub>). *Proc. Natl Acad. Sci. USA* **113**, 11420–11424 (2016).
11. Albertini, O. R. et al. Zone-center phonons of bulk, few-layer, and monolayer 1T-TaS<sub>2</sub>: detection of commensurate charge density wave phase through Raman scattering. *Phys. Rev. B* **93**, 214109 (2016).
12. Hellmann, S. et al. Ultrafast melting of a charge-density wave in the Mott insulator 1T-TaS<sub>2</sub>. *Phys. Rev. Lett.* **105**, 187401 (2010).
13. Stojchevska, L. et al. Ultrafast switching to a stable hidden quantum state in an electronic crystal. *Science* **344**, 177–180 (2014).
14. Eichberger, M. et al. Snapshots of cooperative atomic motions in the optical suppression of charge density waves. *Nature* **468**, 799–802 (2010).

15. Chi, Z. H. et al. Pressure-induced metallization of molybdenum disulfide. *Phys. Rev. Lett.* **113**, 036802 (2014).
16. Nayak, A. P. et al. Pressure-modulated conductivity, carrier density, and mobility of multi layered tungsten disulfide. *ACS Nano* **9**, 9117–9123 (2015).
17. Zhao, Z. et al. Pressure induced metallization with absence of structural transition in layered molybdenum diselenide. *Nat. Commun.* **6**, 7312 (2015).
18. Freitas, D. C. et al. Strong enhancement of superconductivity at high pressures within the charge-density-wave states of 2H-TaS<sub>2</sub> and 2H-TaSe<sub>2</sub>. *Phys. Rev. B* **93**, 184512 (2016).
19. Kusmartseva, A. F., Sipos, B., Berger, H., Forro, L. & Tutis, E. Pressure induced superconductivity in pristine 1T-TaSe<sub>2</sub>. *Phys. Rev. Lett.* **103**, 236401 (2009).
20. Sipos, B. et al. From Mott state to superconductivity in 1T-TaS<sub>2</sub>. *Nat. Mater.* **7**, 960–965 (2008).
21. Wang, B. S. et al. Pressure-induced bulk superconductivity in a layered transition-metal dichalcogenide 1T-tantalum selenium. *Phys. Rev. B* **95**, 220501 (2017).
22. Qi, Y. P. et al. Superconductivity in Weyl semimetal candidate MoTe<sub>2</sub>. *Nat. Commun.* **7**, 11038 (2016).
23. Guguchia, Z. et al. Signatures of the topological s<sup>±</sup> superconducting order parameter in the type-II Weyl semimetal T<sub>d</sub>-MoTe<sub>2</sub>. *Nat. Commun.* **8**, 1082 (2017).
24. Cai, P. L. et al. Drastic pressure effect on the extremely large magnetoresistance in WTe<sub>2</sub>: quantum oscillation study. *Phys. Rev. Lett.* **115**, 057202 (2015).
25. Pan, X. C. et al. Pressure-driven dome-shaped superconductivity and electronic structural evolution in tungsten ditelluride. *Nat. Commun.* **6**, 7805 (2015).
26. Liu, A. Y. Electron-phonon coupling in compressed 1T-TaS<sub>2</sub>: stability and superconductivity from first principles. *Phys. Rev. B* **79**, 220515 (2009).
27. Ravy, S. et al. High-pressure X-ray diffraction study of 1T-TaS<sub>2</sub>. *Physica. B Condens. Matter* **407**, 1704–1706 (2012).
28. Ritschel, T. et al. Pressure dependence of the charge density wave in 1T-TaS<sub>2</sub> and its relation to superconductivity. *Phys. Rev. B* **87**, 125135 (2013).
29. Chi, Z. H. et al. Superconductivity in pristine 2H<sub>s</sub>-MoS<sub>2</sub> at ultrahigh pressure. *Phys. Rev. Lett.* **120**, 037002 (2018).
30. Zhou, D. W. et al. Pressure-induced metallization and superconducting phase in ReS<sub>2</sub>. *npj Quantum Mater.* **2**, 19 (2017).
31. Wang, Y. C., Lv, J. A., Zhu, L. & Ma, Y. M. Crystal structure prediction via particle-swarm optimization. *Phys. Rev. B* **82**, 094116 (2010).
32. Wang, Y. C., Lv, J., Zhu, L. & Ma, Y. M. CALYPSO: A method for crystal structure prediction. *Comput. Phys. Commun.* **183**, 2063–2070 (2012).
33. Giannozzi, P. et al. QUANTUM ESPRESSO: a modular and open-source software project for quantum simulations of materials. *J. Phys. Condens. Matter* **21**, 395502 (2009).
34. Allen, P. B. & Dynes, R. C. Transition temperature of strong-coupled superconductors reanalyzed. *Phys. Rev. B* **12**, 905–922 (1975).
35. Yu, Y. G. G. & Ross, N. L. First-principles study on thermodynamic properties and phase transitions in TiS<sub>2</sub>. *J. Phys. Condens. Matter* **23**, 055401 (2011).
36. Liu, Z. L., Cai, L. C. & Zhang, X. L. Novel high pressure structures and superconductivity of niobium disulfide. *J. Alloys Compd.* **610**, 472–477 (2014).
37. Kohulák, O. & Martoňák, R. New high-pressure phases of MoSe<sub>2</sub> and MoTe<sub>2</sub>. *Phys. Rev. B* **95**, 054105 (2017).
38. Liu, Z. L., Jia, H., Li, R., Zhang, X. L. & Cai, L. C. Unexpected coordination number and phase diagram of niobium diselenide under compression. *Phys. Chem. Chem. Phys.* **19**, 13219–13229 (2017).
39. Zhou, D. et al. Evolution of crystal structures and electronic properties for TiS<sub>2</sub> at high pressure. *J. Alloys Compd.* **757**, 448–454 (2018).
40. Kohulák, O., Martoňák, R. & Tosatti, E. High-pressure structure, decomposition, and superconductivity of MoS<sub>2</sub>. *Phys. Rev. B* **91**, 144113 (2015).
41. Suderow, H., Tissen, V. G., Brison, J. P., Martinez, J. L. & Vieira, S. Pressure induced effects on the Fermi surface of superconducting 2H-NbSe<sub>2</sub>. *Phys. Rev. Lett.* **95**, 117006 (2005).
42. Boaknin, E. et al. Heat conduction in the vortex state of NbSe<sub>2</sub>: evidence for multiband superconductivity. *Phys. Rev. Lett.* **90**, 117003 (2003).
43. Huang, C. L. et al. Experimental evidence for a two-gap structure of superconducting NbSe<sub>2</sub>: a specific-heat study in external magnetic fields. *Phys. Rev. B* **76**, 212504 (2007).
44. Morosan, E. et al. Superconductivity in Cu<sub>x</sub>TiSe<sub>2</sub>. *Nat. Phys.* **2**, 544–550 (2006).
45. Vanderbilt, D. Soft self-consistent pseudopotentials in a generalized eigenvalue formalism. *Phys. Rev. B* **41**, 7892 (1990).
46. Perdew, J. P., Burke, K. & Ernzerhof, M. Generalized gradient approximation made simple. *Phys. Rev. Lett.* **77**, 3865 (1996).
47. Dynes, R. C. McMillan's equation and the T<sub>c</sub> of superconductors. *Solid State Commun.* **10**, 615 (1972).

## ACKNOWLEDGEMENTS

The authors acknowledge support from the National Key R&D Program of China (2018YFA0305900, 2016YFA0300404), NSFC (11874172, 11374120, 11634004, 51320105007, 11674326, 11874357, U2032215, U1932217 and U1832141), and JLU Science and Technology Innovative Research Team (2017TD-01).

## AUTHOR CONTRIBUTIONS

Q.D., Q.L., and B.L. designed the research. X.L. and Y.S. grew the single crystal. Q.D. performed the high-pressure XRD experiment. Q.D. and S.L. performed the high-pressure electrical transport measurements. R.L. and B.L. assisted the high-pressure experiments. X.S., S.N., S.L., J.S., and W.L. performed the calculations. Q.D., Q.L., J.S., W.L., N.H., and B.L. contributed to analyze the data. Q.D. and Q.L. wrote the paper.

## COMPETING INTERESTS

The authors declare no competing interests.

## ADDITIONAL INFORMATION

**Supplementary information** The online version contains supplementary material available at <https://doi.org/10.1038/s41535-021-00320-x>.

**Correspondence** and requests for materials should be addressed to Q.L., Y.S. or B.L.

**Reprints and permission information** is available at <http://www.nature.com/reprints>

**Publisher's note** Springer Nature remains neutral with regard to jurisdictional claims in published maps and institutional affiliations.



**Open Access** This article is licensed under a Creative Commons Attribution 4.0 International License, which permits use, sharing, adaptation, distribution and reproduction in any medium or format, as long as you give appropriate credit to the original author(s) and the source, provide a link to the Creative Commons license, and indicate if changes were made. The images or other third party material in this article are included in the article's Creative Commons license, unless indicated otherwise in a credit line to the material. If material is not included in the article's Creative Commons license and your intended use is not permitted by statutory regulation or exceeds the permitted use, you will need to obtain permission directly from the copyright holder. To view a copy of this license, visit <http://creativecommons.org/licenses/by/4.0/>.

© The Author(s) 2021